International Journal of Minerals, Metallurgy and Materials
Volume 27, Number 8, August 2020, Page 1083
https://doi.org/10.1007/s12613-019-1957-8

Influence of crucible material on inclusions in 95Cr saw-wire steel deoxidized by Si–Mn

Yang Li, Chang-yong Chen, Guo-qing Qin, Zhou-hua Jiang, Meng Sun, and Kui Chen

School of Metallurgy, Northeasten University, Shenyang 110819, China
(Received: 6 July 2019; revised: 17 November 2019; accepted: 19 November 2019)

Abstract: To investigate the interaction mechanism between 95Cr saw-wire steel and different refractories, we conducted laboratory experiments at 1873 K. Five crucible materials (SiO_2, Al_2O_3, $MgO·Al_2O_3$, MgO, and MgO–CaO) were used. The results indicate that SiO_2, Al_2O_3, and $MgO·Al_2O_3$ are not suitable for smelting low-oxygen, low-$[Al]_s$ 95Cr saw-wire steel, mainly because they react with the elements in the molten steel and pollute the steel samples. By contrast, MgO–CaO is an ideal choice to produce 95Cr saw-wire steel. It offers three advantages: (i) It does not decompose by itself at the steelmaking temperature of 1873 K because it exhibits good thermal stability; (ii) [C], [Si], and [Mn] in molten steel cannot react with it to increase the [O] content; and (iii) it not only desulfurizes and dephosphorizes but also removes Al_2O_3 inclusions from the steel simultaneously. As a result, the contents of the main elements ([C], [Si], [Mn], [Cr], N, T.O (total oxygen)) in the steel are not affected and the content of impurity elements ($[Al]_s$, P, and S) can be perfectly controlled within the target range. Furthermore, the number and size of inclusions in the steel samples decrease sharply when the MgO–CaO crucible is used.

Keywords: nonmetallic inclusions; 95Cr saw-wire steel; crucible material; MgO–CaO refractory

1. Introduction

Saw wire is an ultrafine steel wire with a diameter between 50 and 80 μm. It was developed on the basis of steel cord and is used to cut gemstones or silicon wafers. If the saw wire breaks during cutting, the whole material is discarded. Therefore, the breakage rate of saw wire should be minimized.

Inclusions with diameters larger than 5 μm should be removed from saw wire because they often function as breakage initiation points when the wire is subjected to cold drawing and cyclic stress [1]. Numerous technologies have been investigated for controlling inclusions in tire-cord steel and saw-wire steel, including the selection of a suitable steel deoxidizer [2–4], the development of new refining slag systems [5–7], the modification of inclusions in steel via microalloying [8–12], and improvements in the smelting process [13]. However, little research has been reported on the effect of refractories on inclusions in tire-cord steel and saw-wire steel, especially in the past decade. Table 1 presents a summary of the relevant research reported on this issue over the past ten years.

Clearly, many issues have not been sufficiently researched, although the types of refractories have been comprehensively studied. The most important remaining issue is the mechanism by which different refractories influence inclusions [14–16]. In addition, a controversy over whether Al-containing refractories will increase the $[Al]_s$ (acid soluble aluminum) content in steel, as indicated by some authors [17–19], remains unresolved.

Therefore, in the current study, laboratory-scale experiments for modifying inclusions using crucibles composed of five different materials (SiO_2, Al_2O_3, $MgO·Al_2O_3$, MgO, and MgO–CaO) were conducted with a $MoSi_2$ furnace. The influence of refractories on the number, size, morphology, and composition distribution of inclusions was studied in depth. In particular, thermodynamic analyses are discussed comprehensively. Furthermore, the modes of interaction between molten steel and refractories are summarized.

2. Experimental

2.1. Experimental apparatus and procedure

Laboratory experiments were designed to study the effect of the crucible material on inclusions in 95Cr saw-wire steel. A schematic of the experimental apparatus is shown in Fig. 1.

Corresponding authors: Chang-yong Chen E-mail: chency@stumail.neu.edu.cn; Zhou-hua Jiang E-mail: jiangzh@smm.neu.edu.cn

Table 1. Reported studies on the effect of refractories on inclusions in tire-cord steel or saw-wire steel in the past decade

Main composition	Summary	Deficiencies (questions not studied in depth)	Ref.
Al_2O_3·MgO	Al_2O_3-containing refractories have no significant effect on the $[Al]_s$ content in tire-cord steel.	The number, morphology, size, and chemical composition distribution of Al_2O_3-containing inclusions were not studied.	[14]
Al_2O_3·MgO, MgO·Al_2O_3, MgO–CaO	The order of the ability of different refractories to improve the cleanliness of molten steel is MgO–CaO > MgO·Al_2O_3 > Al_2O_3·MgO.	The influence of different refractories on the content of impurity element P and Al_2O_3-containing inclusions were not been discussed.	[15]
MgO·Al_2O_3, MgO·Al_2O_3–MgAlON	Increasing the amount of MgAlON in $MgAl_2O_4$ refractories reduces the solubility in molten steel and increases its anti-penetration performance.	The effect of the mechanism of refractories on the number, size, morphology, and chemical composition distribution of inclusions in tire-cord steel were not researched.	[16]
MgO, ZrO_2, SiO_2, Al_2O_3	The order of the ability of different refractories to improve the cleanliness of molten steel is MgO > ZrO_2 > SiO_2 > Al_2O_3.	The reason the Mn content of tire-cord steel decreased sharply when a SiO_2 crucible was used was not discussed.	[17]
Al_2O_3–C	Al_2O_3–C refractory is easily corroded by molten steel and breaks off into molten steel.	The experimental results are not convincing because of the absence of a comparative experiment.	[18]
MgO–C	Al-containing MgO–C refractory should be replaced with Al-free MgO–C refractory because the former tends to increase $[Al]_s$ in tire-cord steel.	The types of refractories studied experimentally are relatively few.	[19]

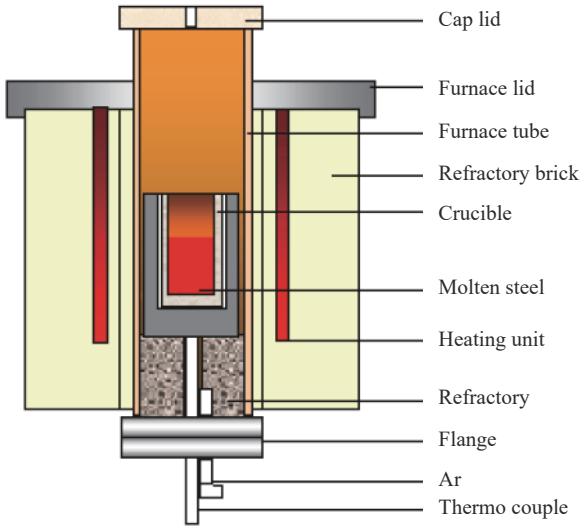

Fig. 1. Schematic of the experimental equipment ($MoSi_2$ furnace).

The target composition of experimental steel is described in Table 2. Notably, C, Si, Mn, and Cr were added during the steelmaking process in the form of alloy, whereas the P, S, $[Al]_s$, and T.O (total oxygen) were brought in by industrial pure iron. Five different refractories were considered in the present study (SiO_2, Al_2O_3, MgO·Al_2O_3, MgO, and MgO–CaO); their chemical compositions are shown in Table 3. All of the crucibles were pressed using a hydraulic press. Specifically, the oxide powers and binder (in this experiment, polyvinyl alcohol ($(C_2H_4O)_n$) aqueous solution was selected as a binder for all of the refractories) were mixed together and then pressed into a mold at a pressure of 20 MPa. The rough crucibles were then sintered at 1783 K for 10800 s.

In the present study, a B-type reference thermocouple was used to measure the temperature of liquid steel. To maintain the oxygen partial pressure as low as possible, high-purity argon (99.999vol%) was introduced into the furnace at a flow rate of 3 L/min, blowing from the bottom to the top of the furnace tube.

The size of the crucibles used in the present experiments was 60 mm inner diameter and 80 mm depth. A graphite crucible was sleeved outside the crucibles to prevent steel leakage during the steelmaking process. The molten steel was maintained 1873 K for 600 s to ensure homogenization, and then the alloying elements were added to the molten steel stepwise. Timing was started from the point when the alloy had completely melted, and the temperature was held constant for 5400 s to ensure adequate contact time between the molten steel and the crucible.

2.2. Analysis methods

The Si, Mn, P, and Cr contents were analyzed by a direct-reading spectrometer. In addition, the Ca and $[Al]_s$ contents were measured by inductively coupled plasma atomic emission spectrometry (ICP-AES) at the Analysis and Testing Center (Chemical Laboratory, Shenyang, China) of Northeastern University. An infrared C/S analyzer and the LECO® TC 500 O_2/N_2 analyzer were used to detect the C, S, T.O, and N contents. The results are shown in Table 4.

Table 2. Target composition of experimental 95Cr saw-wire steel wt%

Target	C	Si	Mn	Cr	P	S	$[Al]_s$	T.O	N
Range	0.94–0.96	0.15–0.25	0.30–0.40	0.15–0.25	≤0.008	≤0.008	≤0.0005	≤0.002	≤0.004
Amount of addition	0.96	0.25	0.40	0.20	0.015	0.008	0.003	0.0013	—

Table 3. Chemical compositions of the selected crucibles wt%

Main material of crucible	Naming of Exp.	MgO	Al_2O_3	CaO	SiO_2	Fe_2O_3	Impurity
SiO_2	S	—	0.2	—	99.5	<0.005	≤0.2
Al_2O_3	A	—	99.7	—	0.04	0.05	≤0.2
$MgO·Al_2O_3$	MA	78.05	18.91	1.06	0.92	—	≤0.2
MgO	M	96.15	0.34	2.40	—	—	≤0.2
MgO–CaO	MC	67.78	1.1	30.26	0.65	—	≤0.2

Table 4. Chemical compositions of 95Cr steel wt%

Exp.	C	Si	Mn	Cr	P	S	$[Al]_s$	Ca	T.O	N
S	0.60	0.35	0.33	0.20	0.0137	0.0053	0.0013	0.0002	0.0037	0.0015
A	0.96	0.12	0.40	0.20	0.0132	0.0056	0.0075	0.0007	0.0031	0.0012
MA	0.92	0.20	0.39	0.20	0.0092	0.0027	0.0043	0.0004	0.0014	0.0009
M	0.96	0.25	0.38	0.20	0.0086	0.0024	≤0.0005	0.0004	0.0010	0.0010
MC	0.95	0.25	0.39	0.20	0.0055	0.0006	≤0.0005	0.0018	0.0005	0.0010

All of the steel samples were prepared using 100–2000 mesh sand papers and polished. Photos (more than 50) in an "S" route were taken with an OLYMPUS metallographic microscope (on the surface of each sample, photos were taken in order from right to left, followed by from left to right). The size and count of inclusions were analyzed using the Image J software (Image J 1.48, National Institutes of Health, Bethesda, MD, USA, 2014; this software is a public domain, Java-based image processing program developed at the NIH). In addition, the morphology and components of inclusions were characterized by scanning electron microscopy (SEM, Carl Zeiss AG, Niedersachsen, Germany) and energy-dispersive spectroscopy (EDS, Carl Zeiss AG, Niedersachsen, Germany).

3. Results

3.1. Composition of experimental steels

The chemical composition of experimental steels is shown in Table 4. The contents of the elements other than Cr and N differ substantially between the target values and experimental values, mainly because of numerous reactions between the molten steel and the crucibles during the steelmaking process.

For Exp. S (SiO_2 crucible), the contents of C and Mn are lower than the target values; by contrast, the Si, P, and T.O contents were enriched. Exp. A (Al_2O_3 crucible) exhibit similar changes, although some differences are observed; in particular, the Si is much lower than the target value, whereas the content of $[Al]_s$ is much higher than the target value. For Exp. MA ($MgO·Al_2O_3$ crucible), almost all of the elements are qualified expect P and $[Al]_s$, which are slightly higher than their target values. For Exp. M (MgO crucible) and Exp. MC (MgO–CaO crucible), the results match the standard very well; specifically, the contents of P, S, $[Al]_s$, and T. O in Exp. MC decreased to only 5.5×10^{-3}wt%, 6×10^{-4}wt%, ≤ 5×10^{-8}wt%, and 5×10^{-4}wt%, respectively.

3.2. Number, size, and composition distribution of inclusions in experimental steels

3.2.1. Influence of crucible material on the number of inclusions

Table 5 shows the effect of the crucible material on the number of nonmetallic inclusions in the experimental steels. Both the density and area ratio of the inclusions sharply decreased with increasing alkalinity of the crucible material. The detection area was 14 mm^2, and the total number of inclusions in the S, A, MA, M, and MC experiments was 933, 725, 642, 563, and 500, respectively; that is, the density of inclusions was 66.6, 51.8, 45.9, 39.4, and 35.7 mm^{-2}, respectively. The density of inclusions thus sharply decreased from 66.6 to 35.7 mm^{-2}. A similar regularity was found for the area ratio of inclusions, which decreased from 0.024% to 0.013%.

3.2.2. Influence of crucible material on the size of inclusions

The effect of crucible material on the size distribution of nonmetallic inclusions in the experimental steels is shown in Table 6. Overall, the size of inclusions decreased with increasing alkalinity of the crucible material. Specifically, the percentage of inclusions smaller than 2 μm in diameter increased sharply from 67wt% (with SiO_2 crucible) to 91wt%

Table 5. Statistical results of inclusions in 95Cr steel

Exp.	Total number of inclusions	View area / mm^2	Density of inclusions / mm^{-2}	Area ratio / %
S	933	14	66.6	0.024
A	725	14	51.8	0.019
MA	642	14	45.9	0.015
M	563	14	39.4	0.014
MC	500	14	35.7	0.013

Table 6. Size distributions of inclusions in 95Cr steel %

Exp.	<1 μm	1–2 μm	2–5 μm	>5 μm	Average diameter / μm
S	26	41	25	8	1.695
A	30	46	18	6	1.543
MA	42	46	10	2	1.293
M	42	47	9	2	1.217
MC	44	47	8	1	1.141

(with MgO–CaO crucible), and the average diameter on non-metallic inclusions decreased markedly from 1.695 μm in Exp. S to 1.141 μm in Exp. MC at the same time.

3.2.3. Influence of crucible material on the composition distribution of inclusions

The composition distribution of inclusions in experimental steels is shown in the pseudo-ternary phase diagram of SiO_2–(MgO + MnO + CaO)–Al_2O_3, which was constructed on the basis of SEM and EDS analyses. The diagram is shown in Fig. 2, where each point represents an inclusion. In addition, the specific composition of typical inclusions in each of the experimental steel samples is listed in Table 7.

The influence of the crucible material on the composition distribution of inclusions was clearly significant. For Exp. S (SiO_2 crucible), most of the inclusions were concentrated in the area with more than 80wt% SiO_2 and the distribution was scattered. For Exp. A, almost all of the inclusions focused on the area with more than 30wt% Al_2O_3, approximately 40wt% SiO_2, and approximately 30wt% (MnO + MgO + CaO). In addition, some inclusions were pure Al_2O_3 inclusions. For wire steels, especially for tire-cord steels and saw-wire steels, pure Al_2O_3 inclusions must be avoided as far as possible because of their poor plasticity, albeit under high temperatures. For Exp. MA, the inclusions mainly deviated from the low-melting-point zone. Specifically, most of the inclusions were concentrated in the area with more than 30wt% Al_2O_3, approximately 40wt% SiO_2, and approximately 30wt% (MnO + MgO + CaO). The distribution of inclusions in Exp. MC was similar to that in Exp. M. Specifically, most of the inclusions were located in the area with less than 20wt% Al_2O_3, approximately 40wt% SiO_2, and approximately 40wt% (MnO + MgO + CaO). In addition, a small amount of inclusions with more than 80wt% SiO_2 were also observed. Compared with Exp. M, the most prominent feature of Exp. MC was that the content of Al_2O_3 in inclusions was mostly less than 10wt%, whereas the content of CaO was relatively greater, as shown in Table 7. Therefore, on the basis of the aforementioned experiments, we reasonably concluded that an alkaline crucible material is helpful to improve the cleanliness of molten steel.

3.2.4. Morphology and element distribution of typical complex oxide inclusions

The morphology and elemental mapping images of typic-

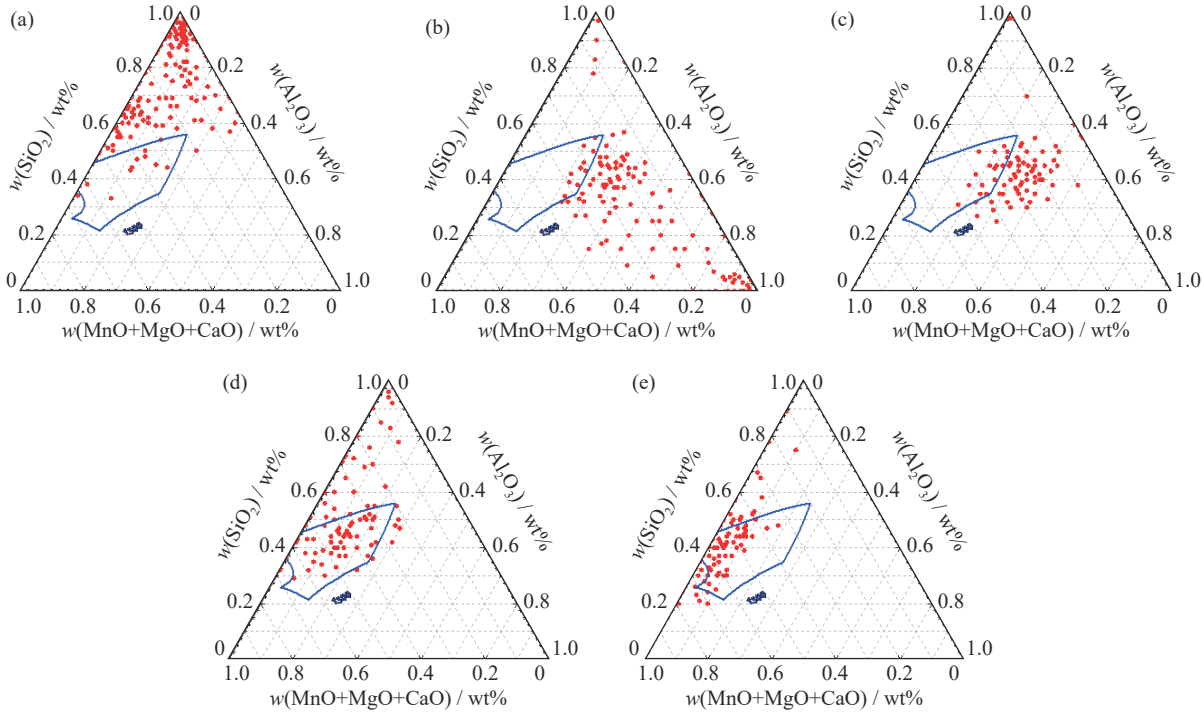

Fig. 2. Effect of crucible material on the composition distribution of inclusions in 95Cr steel: (a) Exp. S; (b) Exp. A; (c) Exp. MA; (d) Exp. M; (e) Exp. MC.

Table 7. Chemical compositions of typical inclusions in experimental steel samples wt%

Exp.	No.	Size / μm	SiO_2	CaO	MnO	MgO	Al_2O_3
S (SiO_2 crucible)	1	3.8	52	2	27	8	11
	2	2.7	70	2	14	4	10
	3	8.7	87	1	5	2	5
	4	2.9	76	3	7	3	11
	5	3.3	75	0	22	0	3
	6	6.4	81	0	16	0	3
	7	14.3	100	0	0	0	0
	8	5.1	67	0	33	0	0
	9	47.3	99	1	0	0	0
	10	2.3	100	0	0	0	0
	11	2.7	81	0	0	0	19
	12	4.8	86	0	0	0	14
	13	3.1	85	0	0	0	15
	14	14.7	93	0	3	0	4
A (Al_2O_3 crucible)	1	7.3	0	0	0	0	100
	2	5.6	16	4	19	2	59
	3	3.5	26	0	0	0	74
	4	2.4	45	2	19	0	34
	5	1.9	10	0	18	3	69
	6	2.8	39	2	28	0	31
	7	8.9	44	2	30	0	24
	8	3.8	32	1	27	0	40
	9	7.3	33	1	25	0	41
	10	2.5	45	6	5	5	39
	11	3.1	48	8	7	3	34
MA ($MgO·Al_2O_3$ crucible)	1	8.9	44	2	15	8	31
	2	2.3	55	0	30	1	14
	3	5.0	34	1	13	12	40
	4	6.1	52	2	14	5	27
	5	0.9	56	0	14	7	23
	6	11.2	35	1	18	14	32
	7	5.1	54	0	28	2	16
	8	4.7	37	0	50	2	11
	9	3.1	45	4	17	0	34
	10	8.3	47	1	34	4	14
	11	6.8	55	1	15	8	21
M (MgO crucible)	1	2.7	70	1	21	2	6
	2	3.1	60	0	30	1	9
	3	0.9	51	1	26	3	19
	4	1.3	44	3	31	2	20
	5	4.2	29	2	62	2	5
	6	1.6	33	4	46	3	14
	7	1.0	48	1	41	5	5
	8	1.3	47	0	39	3	11
	9	5.7	41	0	50	2	7
	10	0.8	75	1	11	4	9
	11	1.1	92	0	3	1	4
	12	1.0	90	0	9	1	0
MC (MgO–CaO crucible)	1	1.6	44	18	22	6	10
	2	2.8	48	11	33	1	7
	3	1.3	60	10	7	18	5
	4	5.1	20	5	74	0	1
	5	0.9	21	12	62	2	3
	6	0.7	37	6	47	3	7
	7	1.1	50	11	28	9	2
	8	1.2	100	0	0	0	0
	9	2.4	39	3	48	7	3
	10	1.0	76	1	10	11	2

al nonmetallic inclusions in each experiment are presented in Figs. 3–12. As shown in Figs. 3 and 4, the main types of inclusions in Exp. S are multiphase composite oxide inclusions larger than 5 μm and containing more than 80wt% SiO_2. In

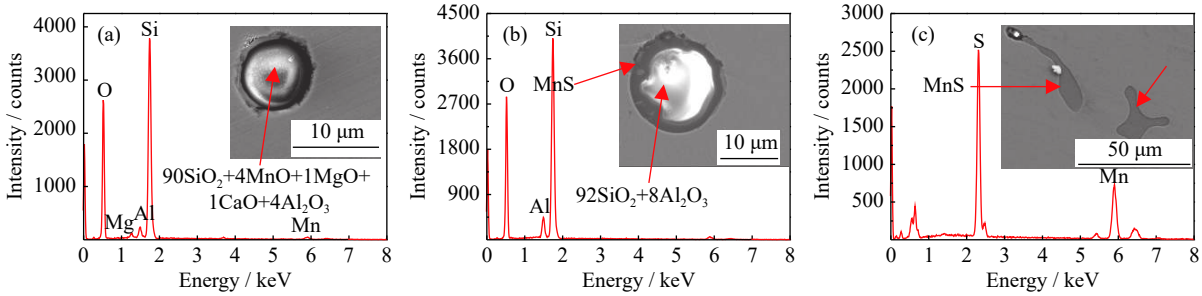

Fig. 3. Typical inclusions in Exp. S (SiO_2 crucible): (a) $90SiO_2 + 4MnO + 1MgO + 1CaO + 4Al_2O_3$; (b) $92SiO_2 + 8Al_2O_3$; (c) MnS.

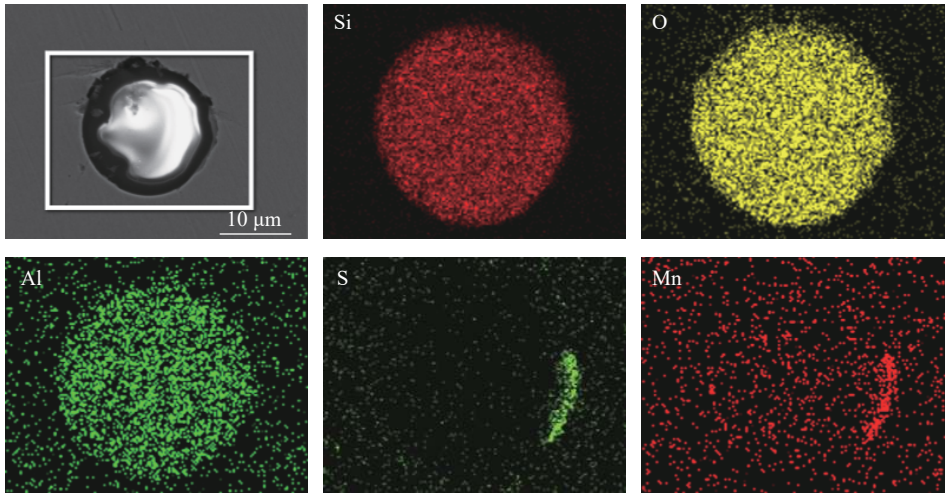

Fig. 4. SEM mapping images of typical inclusions in Exp. S (SiO_2 crucible).

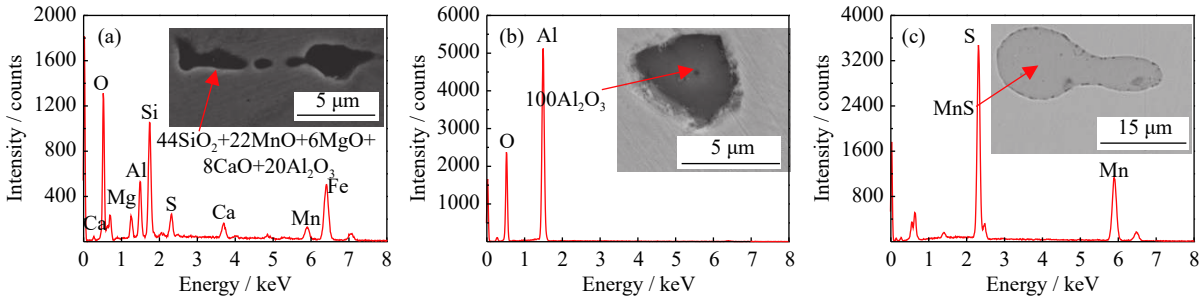

Fig. 5. Typical inclusions in Exp. A (Al_2O_3 crucible): (a) $44SiO_2 + 22MnO + 6MgO + 8CaO + 20Al_2O_3$; (b) $100Al_2O_3$; (C) MnS.

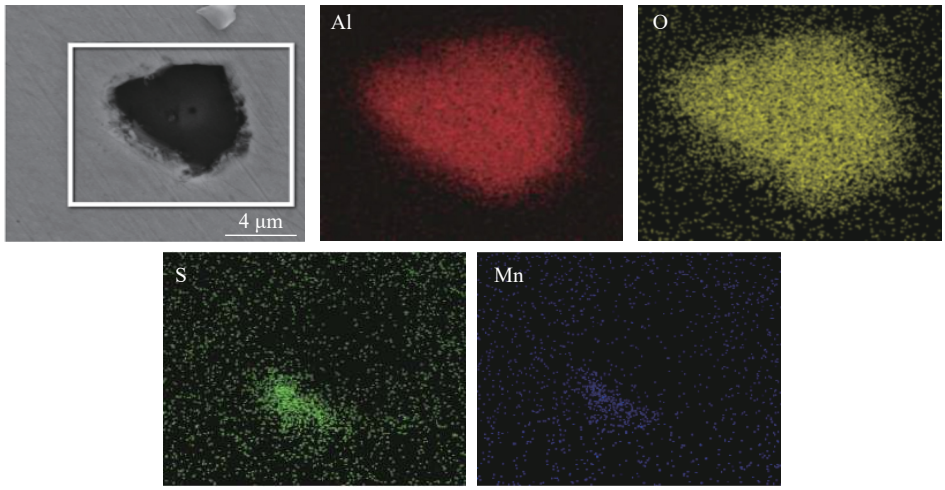

Fig. 6. SEM mapping images of typical inclusions in Exp. A (Al_2O_3 crucible).

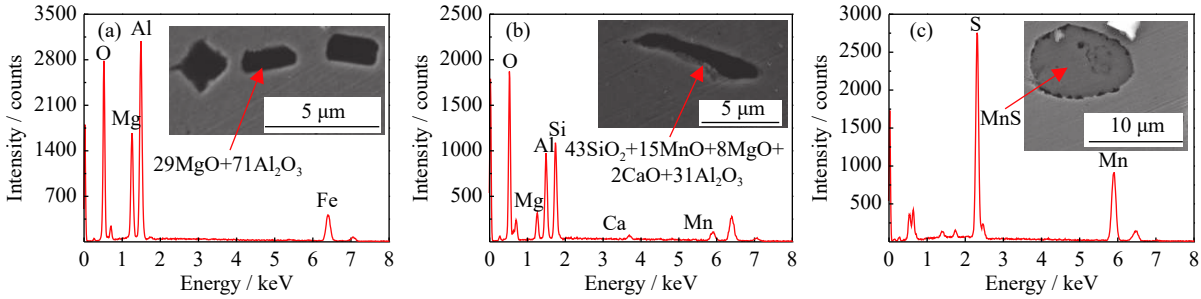

Fig. 7. Typical inclusions in Exp. MA ($MgO·Al_2O_3$ crucible): (a) $29MgO + 71Al_2O_3$; (b) $43SiO_2 + 15MnO + 8MgO + 2CaO + 31Al_2O_3$; (c) MnS.

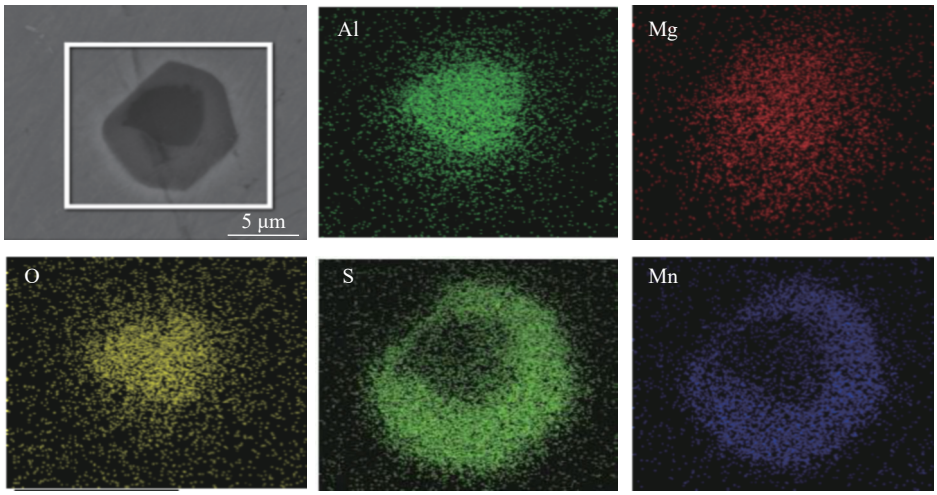

Fig. 8. SEM mapping images of typical inclusions in Exp. MA ($MgO·Al_2O_3$ crucible).

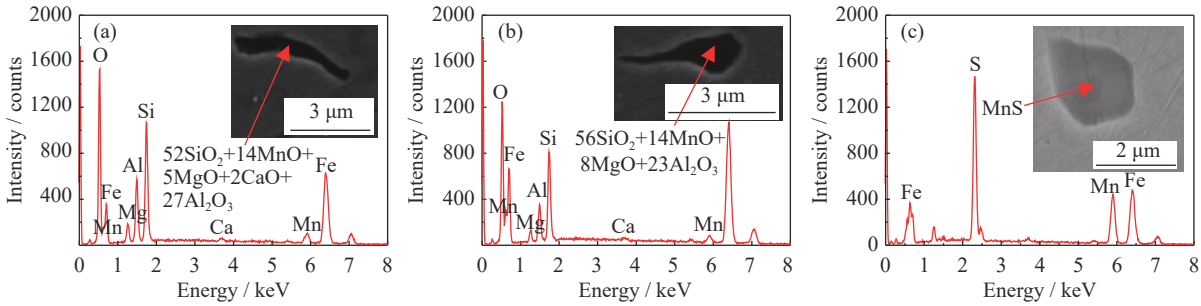

Fig. 9. Typical inclusions in Exp. M (MgO crucible): (a) $52SiO_2 + 14MnO + 5MgO + 2CaO + 27Al_2O_3$; (b) $56SiO_2 + 14MnO + 8MgO + 23Al_2O_3$; (c) MnS.

general, most of these inclusions are spherical, with the edge wrapped by a layer of MnS, as shown in Fig. 4. Uniphase MnS inclusions consistently exhibit a large size and irregular shape, as shown in Fig. 3(c).

Typical inclusions in Exp. A with a high mass fraction of Al_2O_3 are shown in Figs. 5 and 6. These Al_2O_3 inclusions exhibit irregular geometries with sharp corners, and they are larger than 5 μm. Because of these inclusions' poor deformability, they often act as a point of origin of breaks in wires used in working situations. Almost all of the single-phase MnS inclusions are larger than 10 μm and exhibit irregular shapes such as strips and ellipsoids.

Spinel inclusions are the typical inclusion type in Exp. MA, shown in Fig. 7 and Fig. 8. The spinel inclusions typically exhibit irregular geometries with sharp corners. The size and morphology of single-phase MnS inclusions are similar to those in Exp. S.

Typical nonmetallic inclusions in Exp. MC are similar to those in Exp. M. For Exp. MC, the content of CaO in inclusions is much greater than that in the other experimental steel samples. The uniphase MnS inclusions are mainly 1 μm in size and exhibit spherical, ellipsoidal, triangular, or rectangular shapes.

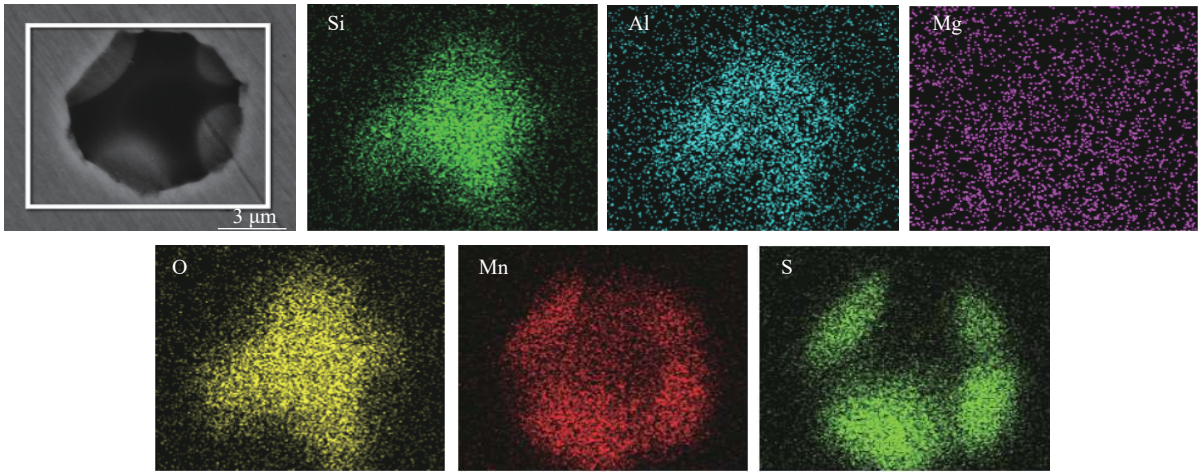

Fig. 10. SEM mapping images of typical inclusions in Exp. M (MgO crucible).

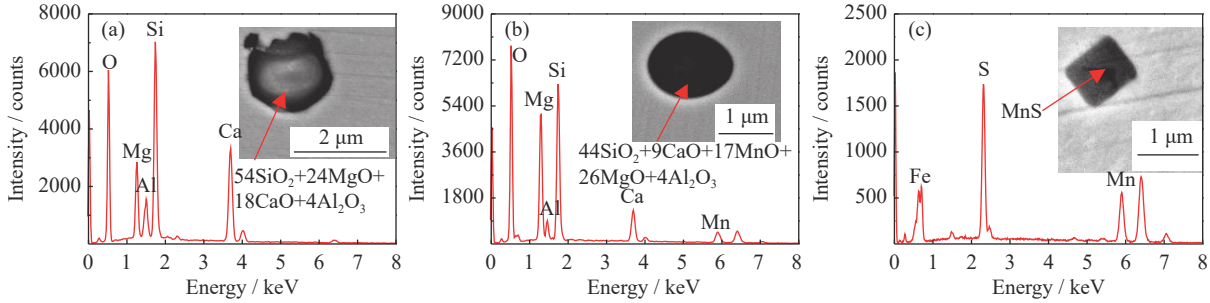

Fig. 11. Typical inclusions in Exp. MC (MgO–CaO crucible): (a) $54SiO_2 + 24MgO + 18CaO + 4Al_2O_3$; (b) $44SiO_2 + 9CaO + 17MnO + 26MgO + 4Al_2O_3$; (c) MnS.

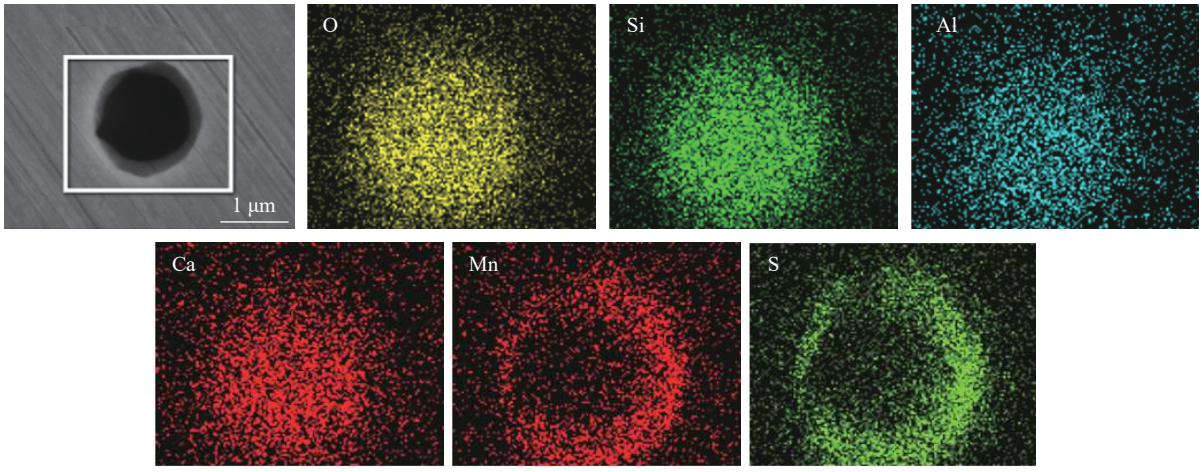

Fig. 12. Typical inclusions in Exp. MC (MgO–CaO crucible).

3.3. Microstructure and phase composition of crucible after interaction with molten steel

3.3.1. SiO_2 crucible

The micromorphology of the SiO_2 crucible after its interaction with 95Cr molten steel is shown in Fig. 13. Obviously, the structure of crucible that after interaction with molten steel can be divided into the original brick layer and a reaction layer; the reaction layer appears as the gray–white region in the SEM micrograph in Fig. 13. The chemical com-

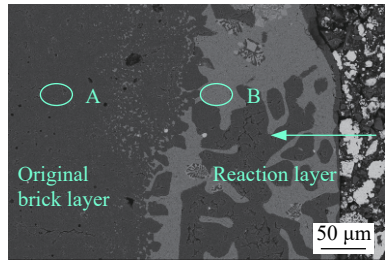

Fig. 13. SEM image of the cross section at one-half the height of the SiO_2 crucible after it interacted with 95Cr molten steel.

position of the two layers was analyzed by EDS; the results are shown in Table 8. The contents of Fe, Ca, Mn, and C in the reaction layer are clearly much higher than those in the original brick layer, which means that the molten steel permeated into the crucible wall during the steelmaking process. This interpretation is validated by the line-scan results in Fig. 14 and the elemental mapping results in Fig. 15.

3.3.2. Al_2O_3 crucible

The micromorphology of the Al_2O_3 crucible after it interacted with 95Cr molten steel was similar to that of the original crucible, as shown in Fig. 16. But, the chemical compositions of the reaction layer and the original brick layer were still different, although their boundary was not obvious according to the EDS analysis results in Table 9 and the mapping scan results in Fig. 17. Specifically, the contents of Fe, Mn, Mg, Ca, and C in points B and C were much higher than those in the original brick layer. In addition, Fe and Ca were concentrated in the boundary layer of crucible, as shown in

Table 8. Element mass fractions in selected positions of the SiO_2 crucible in Fig. 13 wt%

Position	O	Si	Fe	Ca	Mn	C
A	48.71	51.29	—	—	—	—
B	34.25	20.95	13.88	5.01	17.56	8.36

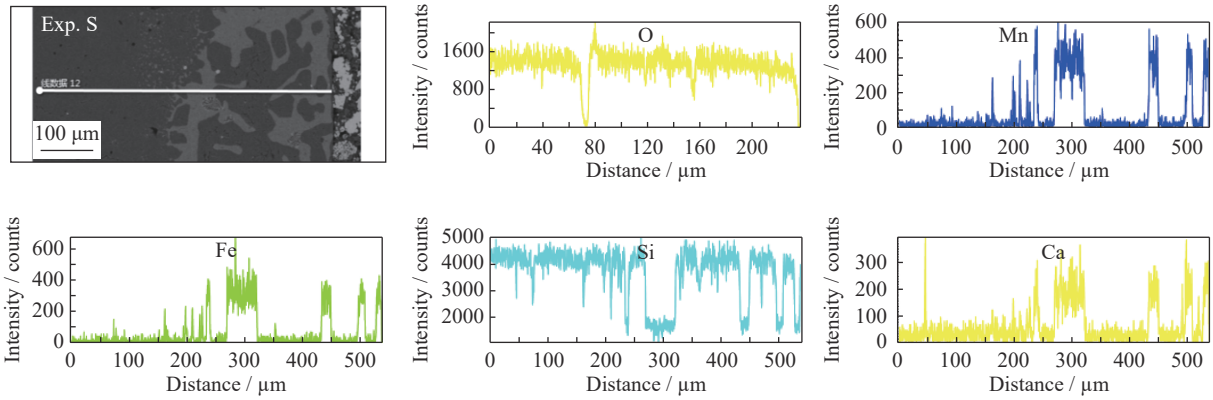

Fig. 14. Line-scan results of the erosion interface of the SiO_2 crucible.

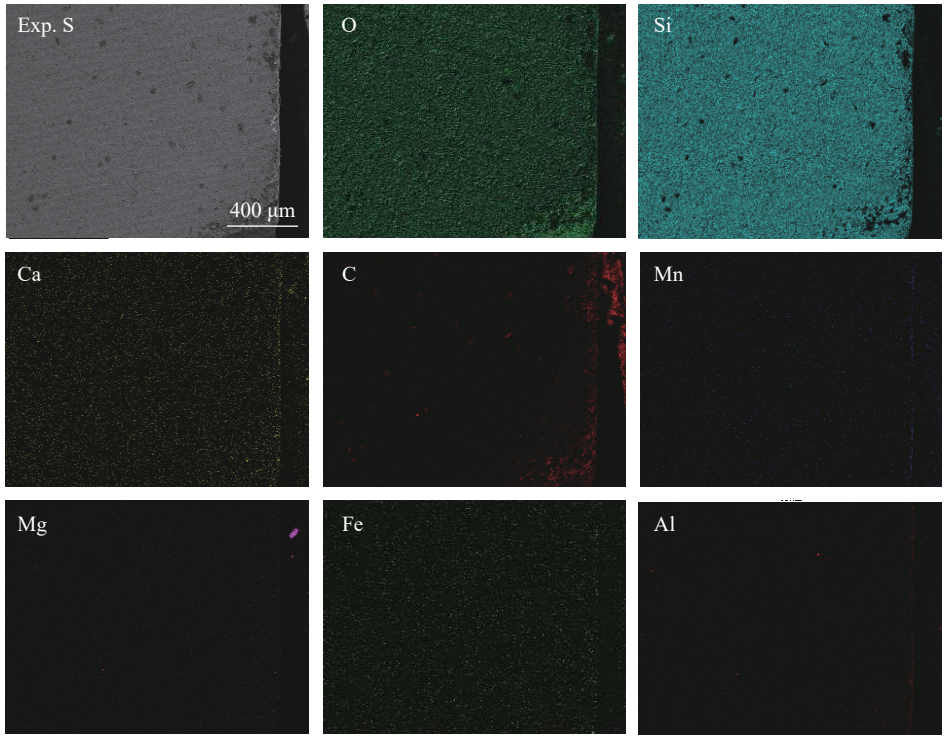

Fig. 15. Elemental mapping results for the SiO_2 crucible.

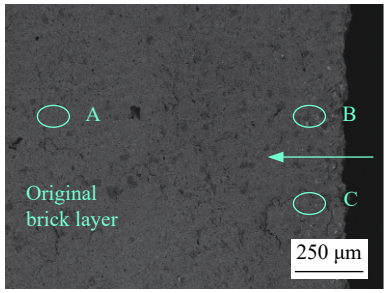

Fig. 16. SEM image of the cross section at one-half the height of the Al_2O_3 crucible after it interacted with 95Cr molten steel.

Fig. 17.

3.3.3. $MgO·Al_2O_3$ crucible

The micromorphology at the one-half-height position of the $MgO·Al_2O_3$ crucible is shown in Fig. 18. Numerous small gray–white spheres are observed in the reaction layer. The EDS analysis results (Table 10) indicate that these small gray–white spheres are solidified molten steel. Thus, these results imply that molten steel penetrated into the crucible wall through infiltration during the steelmaking process. In addition, numerous cracks observed on the wall of the cru-

Table 9. Element mass fractions in selected positions of the Al_2O_3 crucible in Fig. 16 wt%

Position	O	Al	Fe	Mg	Mn	Ca	C
A	46.45	53.55	—	—	—	—	—
B	33.59	36.40	13.91	0.63	9.78	—	5.69
C	47.76	37.14	0.57	—	0.35	0.92	13.26

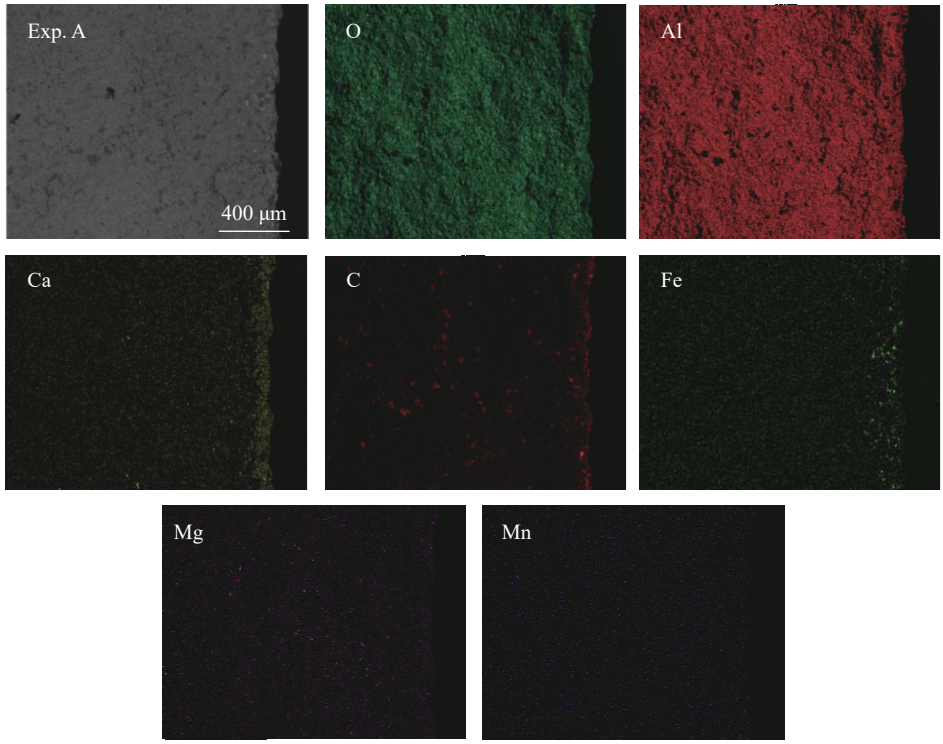

Fig. 17. Elemental mapping images of the Al_2O_3 crucible.

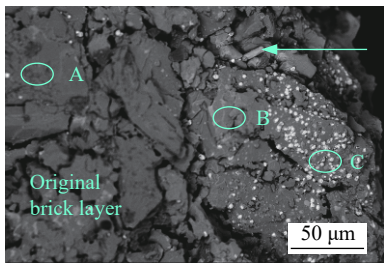

Fig. 18. SEM image of the cross section at one-half the height of the $MgO·Al_2O_3$ crucible after it interacted with 95Cr molten steel.

Table 10. Element mass fractions at selected positions of the $MgO·Al_2O_3$ crucible in Fig. 18 wt%

Position	O	Mg	Fe	Si	Al
A	39.88	60.12	—	—	—
B	44.19	17.68	—	0.30	37.84
C	—	—	100	—	—

cible imply that the refractory may have self-decomposed during the steelmaking process. The elemental mapping results for the $MgO{\cdot}Al_2O_3$ crucible are shown in Fig. 19; the Fe and Si contents in the reaction layer are much greater than those in the original brick layer, whereas the Mg and Al contents exhibit the opposite trend.

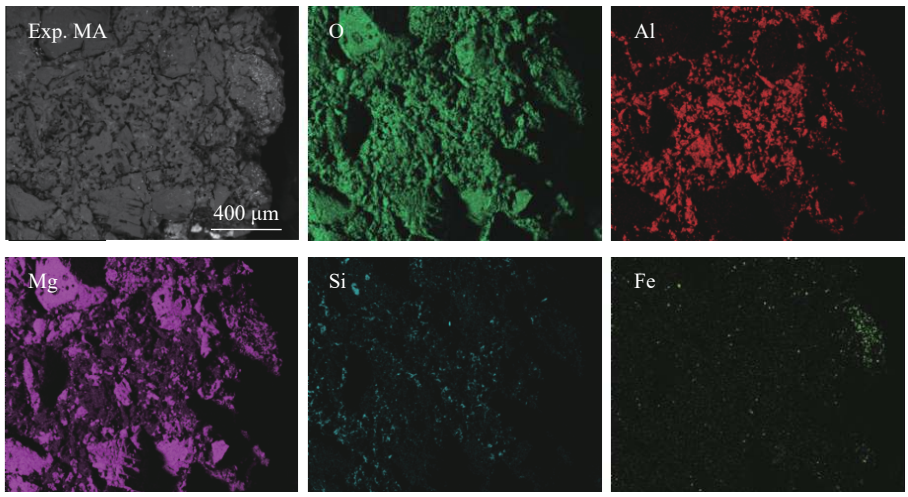

Fig. 19. Elemental mapping images of the $MgO{\cdot}Al_2O_3$ crucible.

3.3.4. MgO crucible

The results of Exp. M (MgO crucible) are shown in Fig. 20, Table 11, and Fig. 21. The Si, Mn, and Ca contents in the reaction layer are higher than in the original brick layer. The structure of the crucible is very compact, implying that a decomposition reaction may not have occurred during the steelmaking process.

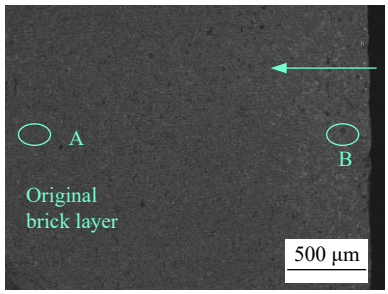

Fig. 20. SEM image of the cross section at one-half the height of the MgO crucible after it interacted with 95Cr molten steel.

3.3.5. MgO–CaO crucible

The micromorphology of the MgO–CaO crucible after it interacted with 95Cr molten steel is shown in Fig. 22. No obvious boundary is observed between the original layer and the reaction layer of the crucible. In addition, no gray–white solidified small steel beads are observed in the reaction layer.

Table 11. Element mass fractions at selected positions of the MgO crucible in Fig. 20 wt%

Position	O	Mg	Fe	Si	Mn	Ca
A	43.2	56.7	—	0.1	—	—
B	41.0	30.67	—	11.8	9.0	7.53

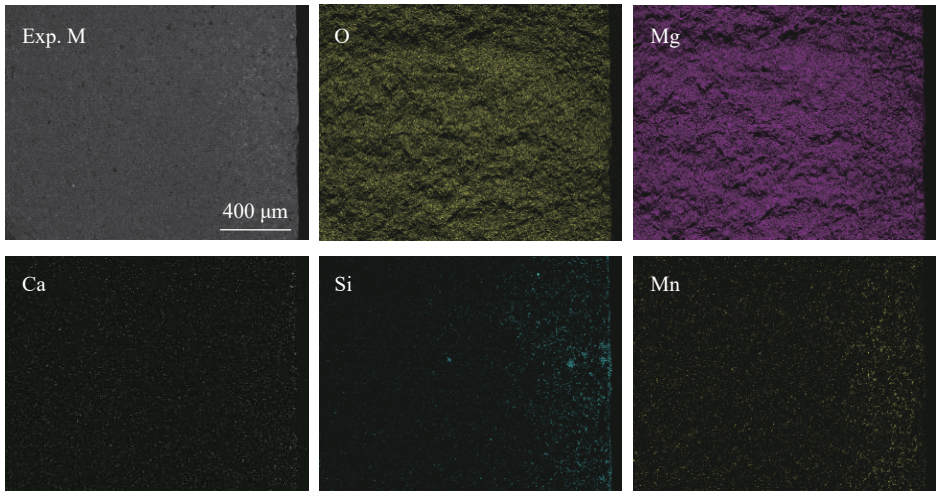

Fig. 21. Elemental mapping images of the MgO crucible.

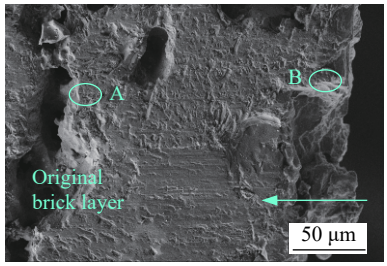

Fig. 22. SEM image of the cross section at one-half the height of the MgO–CaO crucible after it interacted with 95Cr molten steel.

The chemical composition at points A and B of the crucible are shown in Table 12. The results indicate that the Mg and Ca contents at point B are much lower than those at point A, whereas the Al and Si contents exhibit the opposite trend, as shown in Fig. 23.

Table 12. Element mass fractions at selected positions of the MgO–CaO crucible in Fig. 22 wt%

Position	O	Mg	Al	Si	Ca
A	40.98	11.08	—	2.26	45.68
B	51.36	4.23	19.34	16.62	8.45

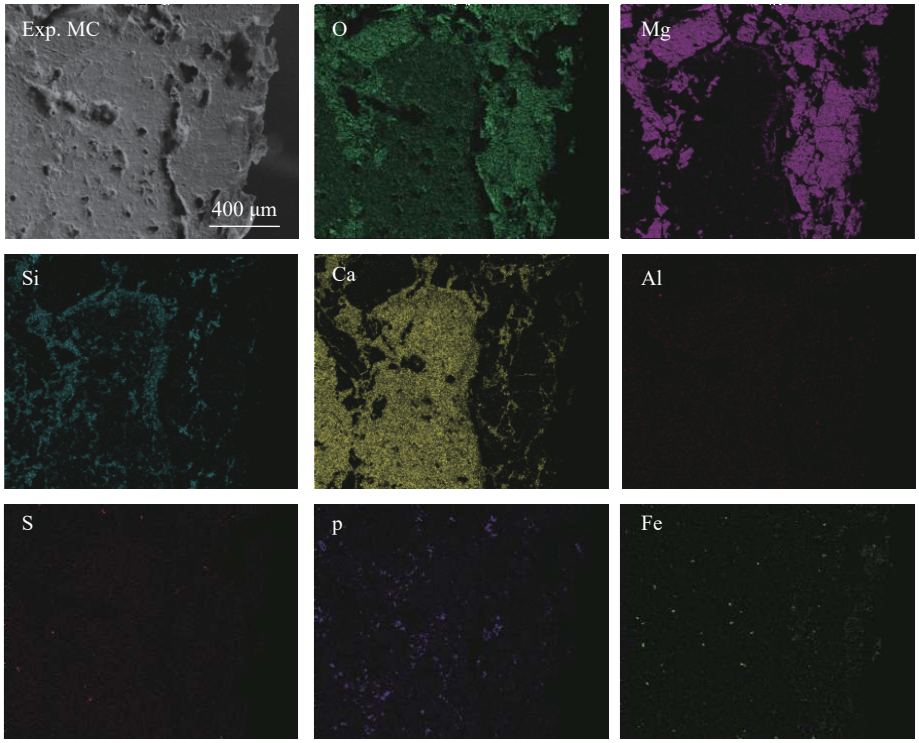

Fig. 23. Elemental mapping images of the MgO–CaO crucible.

4. Discussion

In general, molten steel and refractories can interact three ways [20]:

(i) Refractories decompose and enter into the molten steel under high temperatures during steelmaking.

(ii) Chemical reactions occur between the molten steel and the refractories.

(iii) The molten steel penetrates into the refractories.

4.1. Solution equilibrium thermodynamics of the crucible material

In the present study, the main oxides in the crucible materials were SiO_2, Al_2O_3, MgO + Al_2O_3 + MgO·Al_2O_3, MgO, and MgO + CaO, respectively. The dissolution reactions for these oxides are shown in Table 13, all of them can be described as general expressions Eq. (6) and Eq. (7). Furthermore, the dissolution equilibrium concentration products $a^x_{[M]} \cdot a^y_{[O]}$ can be calculated according to Eq. (7); the results

Table 13. Oxide dissolution reaction equations for various refractories [21]

Eq.	Reaction	$\Delta G^{\ominus}$ / (J·mol^{-1})
(1)	$SiO_2(s) = [Si]_{1\%}+2[O]_{1\%}$	580550–220.66T
(2)	$Al_2O_3(s) = 2[Al]_{1\%}+3[O]_{1\%}$	1205090–387.73T
(3)	$MgO{\cdot}Al_2O_3(s) = MgO(s)+2[Al]_{1\%}+3[O]_{1\%}$	1228694–381.82T
(4)	$MgO(s) = [Mg]_{1\%}+[O]_{1\%}$	484720–147.41T
(5)	$CaO(s) = [Ca]_{1\%}+[O]_{1\%}$	622240–138.42T

Note: $[M]_{1\%}$ means the solution with mass fraction of 1% is used as the standard state when calculating the activity of [M] element.

are shown in Table 14. $a_{[M]}^{x} \cdot a_{[O]}^{y}$ is the equilibrium activity product of chemical reactions; $a_{[M]}^{x}$ and $a_{[O]}^{y}$ are the activity of element [M] and [O], respectively; x and y are the chemical reaction coefficient of element [M] and [O] respectively. The dissolution equilibrium concentration products for MgO and SiO_2 are much greater than those for Al_2O_3, $MgO{\cdot}Al_2O_3$, and CaO. Therefore, MgO and SiO_2 are much more likely to decompose than Al_2O_3, $MgO{\cdot}Al_2O_3$, and CaO at the steelmaking temperature of 1873 K.

In addition, the values of ΔG for Eqs. (1)–(5) are 142.03, 428.76, −7.63, 65.92, and 158.94 kJ/mol (1873 K), respectively (Table 13 and Table 15); thus, all of them are greater than zero except $\Delta G_{(3)}$. Therefore, the $MgO{\cdot}Al_2O_3$ crucible may self-decompose at the steelmaking temperature of 1873 K.

Table 14. Dissolution equilibrium concentration products $a_{[M]}^{x} \cdot a_{[O]}^{y}$ for various oxides at 1873 K

Oxide	$a_{[M]}^{x} \cdot a_{[O]}^{y}$
MgO	1.52×10^{-6}
SiO_2	2.16×10^{-5}
Al_2O_3	4.41×10^{-14}
$MgO{\cdot}Al_2O_3$	4.76×10^{-15}
CaO	7.53×10^{-11}

$$M_xO_y(s) = x[M] + y[O] \quad (6)$$

$$\Delta G_T^{\ominus} = -RT\ln K^{\ominus} = -RT\ln\left(a_{[M]}^{x} \cdot a_{[O]}^{y}\right) \quad (7)$$

Table 15. Interaction coefficients at 1873 K [21]

i, j	Al	Si	Mn	O	P	S	C	Cr	V	Ni
Al	0.043	0.0056	0.0065	–1.867	0.0033	0.03	0.091	0.012	—	–0.0173
Si	0.058	0.11	0.002	–0.23	0.11	0.056	0.18	–0.0003	0.025	0.005
O	–3.9	–0.131	–0.021	–0.2	0.07	–0.133	–0.45	–0.0459	–0.3	0.006
Mn	—	0	0	–0.083	0.0035	–0.048	–0.07	0.0039	0.0057	—
S	0.035	0.053	–0.026	–0.27	0.029	–0.028	0.11	–0.011	–0.016	0
Ca	–0.072	–0.097	–0.0156	–780	–0.097	125	–0.34	0.02	—	–0.044
P	—	0.12	0	—	0.062	0.028	0.13	—	—	0.0002
C	0.043	0.078	–0.012	–0.34	0.051	0.046	0.143	–0.024	–0.077	0.012
Mg	–0.12	–0.09	—	–460	—	–1.38	–0.24	0.05	—	–0.031

4.2. Stability of crucible materials

The effect of temperature on the phase composition of different refractories was calculated using Factsage 7.2 (Bale, C.W.; Pelton, A.D.; Thompson, W.T.; Eriksson, G.; Hack, K.; Chartand, P.; Decterov, S.; Jung, I.H.; Melanson, J.; Petersen, S. Thermfact/CRCT (Montreal, QC, Canada), GTT-Technologies (Aachen, Germany), 2017)); the results are shown in Fig. 24. We focus on the phase composition and change of the crucible material at 1873 K because all of our experiments were carried out at this temperature.

For Exp. S, a slag phase will appear in the SiO_2 refractory when the temperature is increased to 1866 K. Its mass fraction then increases from 0wt% at 1866 K to approximately 4.0wt% at 1873 K. The slag phase easily enters into the molten steel and forms external inclusions. For Exp. A, the crucible material exhibits good stability, as indicated by its lack of an apparent phase transition over the investigated temperature range. For Exp. MA, three phases coexist at 1873 K: MgO, $MgO{\cdot}Al_2O_3$, and slag. As the temperature is increased gradually, the content of $MgO{\cdot}Al_2O_3$ decreases slowly, whereas the transitions of the MgO and slag are completely contrary. For Exp. M, only MgO and MO (M = metal) solid phases coexist at 1873 K; the results indicate that this crucible material exhibits good stability. For Exp. MC, three phases (MgO, CaO, and slag) coexist at 1873 K. The content of the slag phase is stable at ~3wt% in the temperature range from 1773 K to 2023 K. The composition of the slag phase is approximately $38SiO_2$–$30CaO$–$25MgO$–$7Al_2O_3$ according to the material balance calculation. It is a low-melting-point phase in the pseudo-ternary phase diagram of SiO_2–(MgO + MnO + CaO)–Al_2O_3. Therefore, the adverse effects of slag pollution in molten steel are very weak even if the slag phase enters the molten steel.

4.3. Effect of SiO_2 crucible

In Exp. S, the possible chemical reactions between elements in molten steel and refractories are shown in Eqs. (8)–(11). We can determine whether the reactions in Eqs. (8)–(11) can occur by combining the activities of the elements in molten steel and the Van't Hoff equation, $\Delta G = \Delta G^{\ominus} + RT\ln J$. The activity coefficients and activities can be calculated by $\lg f_i = \sum_j e_i^j [\%j]$ and $a_i = f_i[\%i]$, respectively. a_i is the activity of element i; f_i is the activity coefficients element i; e_i^j is the interaction coefficient of elements j to element i; [%i] and [%j] are the mass fraction of element i and j, respectively. The interaction coefficients are shown in Table 15.

$$2[Ca] + SiO_2(s)_{crucible} = 2CaO(s)_{inclusions} + [Si] \quad (8)$$

$$4[Al] + 3SiO_2(s)_{crucible} = 2Al_2O_3(s)_{inclusions} + 3[Si],\ \Delta G^{\ominus} = -658400 + 107.2T\ (J/mol)\ [22-26] \quad (9)$$

$$2[C] + SiO_2(s)_{crucible} = 2CO(g) + [Si],\ \Delta G^{\ominus} = 540870 - 302.270T\ (J/mol)\ [17] \quad (10)$$

$$2[Mn] + SiO_2(s)_{crucible} = 2MnO(s)_{inclusions} + [Si],\ \Delta G^{\ominus} = -17.99 + 0.0268T\ (J/mol)\ [27] \quad (11)$$

Eqs. (8)–(11) are typical oxidation–reduction reactions and will occur at the steelmaking temperature. As a result, the content of Ca in the reaction layer of the crucible is higher than that in the original brick layer, as shown in Fig. 16. For Eq. (10), the value of $\Delta G = -10.9$ kJ/mol < 0 (at 1873 K); thus, it can also occur. For Eq. (11), the activity of MnO is 0.21 [28] because the content of MnO in inclusions was very small; thus, the value of $\Delta G = -20.33$ kJ/mol (at 1873 K) indicates that this reaction will also occur.

In summary, [Ca], [Al], [C], and [Mn] could react with SiO_2 through Eqs. (8)–(11). Consequently, the content of Si increased sharply from 0.25wt% to 0.35wt%, the contents of C and Mn decreased sharply from 0.96wt% to 0.60wt% and from 0.40wt% to 0.33wt%, respectively. Contrasting with these changes, the number and size of inclusions increased sharply, as did the content of SiO_2 in the inclusions.

4.4. Effect of Al_2O_3 crucible

Four chemical reactions can occur between the elements in molten steel and the refractories, as shown in Eqs. (12)–(15) in Exp. A. Eq. (12) occurs at the steelmaking temperature because it is the typical oxidation–reduction reac-

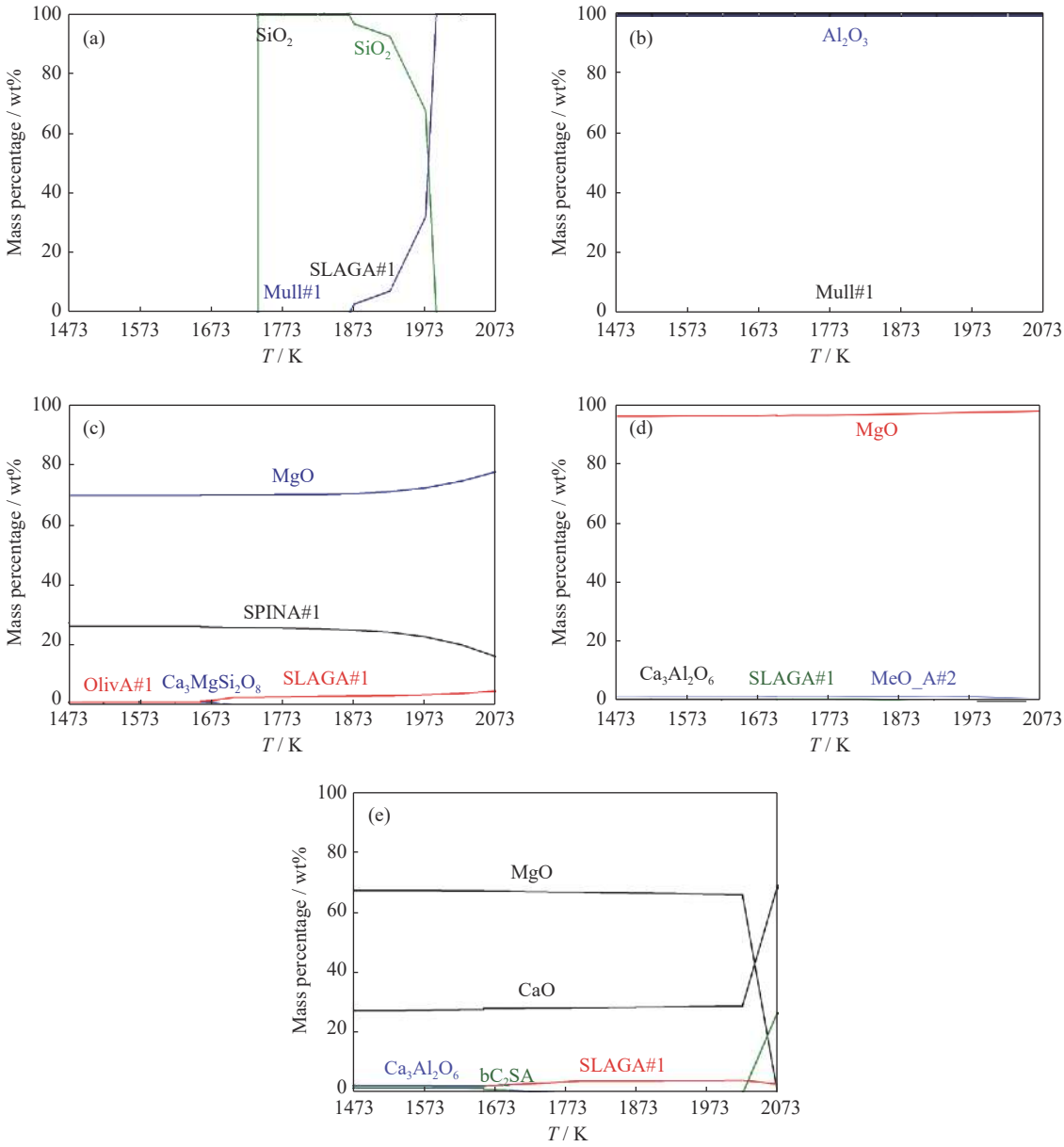

Fig. 24. Effect of temperature on phase composition of different refractories: (a) SiO_2 crucible; (b) Al_2O_3 crucible; (c) $MgO{\cdot}Al_2O_3$ crucible; (d) MgO crucible; (e) MgO–CaO crucible.

tion. Therefore, the content of Ca in the reaction layer at the edge of the crucible was higher than that in other positions, as shown in Fig. 17. For Eq. (13), the value of $\Delta G = -283.63$ kJ/mol (at 1873 K) < 0, which means it can also occur. The occurrence of this reaction explains why the final Si content in the experimental steel samples was reduced to 0.12wt%. The reactions in Eqs. (14) and (15) cannot occur because their ΔG values are 288.24 and 302.67 kJ/mol, respectively. This value indicates that the Al_2O_3 crucible exhibits good chemical stability. Similar results have been reported by and Frank *et al.* [29] and Khanna *et al.* [30–32].

In summary, the content of $[Al]_s$ increased sharply to 7.5×10^{-3}wt%, as the [Ca] and [Si] in molten steel reacted with the Al_2O_3 crucible material. The content of Al_2O_3 in inclusions was therefore much higher than observed in the other experiments, and even some pure Al_2O_3 inclusions were found (Fig. 5).

$$3[Ca] + Al_2O_3(s)_{crucible} = 3CaO(s)_{inclusions} + 2[Al] \quad (12)$$

$$3[Si] + 2Al_2O_3(s)_{crucible} = 3SiO_2(s)_{inclusions} + 4[Al],\ \Delta G^{\ominus} = 621.3 - 0.0972T\ (J/mol)\ [27] \quad (13)$$

$$3[C] + Al_2O_3(s)_{crucible} = 3CO(g) + 2[Al],\ \Delta G^{\ominus} = 1145570 - 509.59T\ (J/mol)\ [14] \quad (14)$$

$$3[Mn] + Al_2O_3(s)_{crucible} = 3MnO(s)_{inclusions} + 2[Al],\ \Delta G^{\ominus} = 337800 - 1.5T\ (J/mol)\ [23-25,33] \quad (15)$$

4.5. Effect of MgO·Al_2O_3 crucible

The main reaction between elements in molten steel and the crucible material in Exp. MA is the dephosphorization of MgO, as shown in Eq. (16). In the initial stage of the reaction, the activity of MgO refractories can be regarded as 1, and that of $Mg_3(PO_4)_2$ is almost zero. The reaction will inevitably proceed to the right to achieve thermodynamic equilibrium, resulting in the P content in the final steel sample being lower than that in Exp. S.

The reaction in Eq. (17) causes the content of $[Al]_s$ to increase slightly. However, the infiltration of molten steel into the crucible wall enables the Al_2O_3-containing refractory particles to easily enter the molten steel. As a result, the content of Al_2O_3 in inclusions increased sharply and almost all of the inclusions were concentrated in the area with a high Al_2O_3 content.

$$2[P] + 5[O] + 3MgO(s)_{crucible} = Mg_3(PO_4)_{2incluisons},\ \Delta G^{\ominus} = -284600 + 142.45T\ (J/mol)\ [34-35] \quad (16)$$

$$3[Ca] + Al_2O_3(s)_{crucible} = 3CaO(s)_{inclusions} + 2[Al] \quad (17)$$

4.6. Effect of MgO crucible

In Exp. M, two chemical reactions occur between the elements in molten steel and refractories, as shown in Eqs. (16) and (18). As a result, the content of P was smaller than those in Exp. S, Exp. A, and Exp. MA. In addition, Ca was enriched on the inner surface of the MgO crucible.

$$[Ca] + MgO(s)_{crucible} = CaO(s)_{inclusions} + Mg \quad (18)$$

4.7. Effect of MgO·CaO crucible

In Exp. MC, both MgO and CaO could function as a dephosphorization agent, as shown in Eqs. (19)–(22).

$$2[P] + 5[O] + 3MgO(s)_{crucible} = Mg_3(PO_4)_{2inclusions},\ \Delta G^{\ominus} = -284600 + 142.45T\ (J/mol)\ [34-35] \quad (19)$$

$$\lg K_{Mg} = 62210/T - 31.14 \quad (20)$$

$$2[P] + 5[O] + 4CaO(s)_{crucible} = Ca_4P_2O_{9inclusions},\ \Delta G^{\ominus} = -343000 + 143.35T\ (J/mol)\ [34-35] \quad (21)$$

$$\lg K_{Ca} = 74970/T - 31.33 \quad (22)$$

where K_{Mg} and K_{Ca} are the reaction equilibrium constant of Eq. (19) and (21), respectively.

Under the same oxygen potential, simultaneous Eqs. (19) and (21) can be obtained:

$$\lg K_{Mg} - \lg K_{Ca} = 2\lg\left([P\%]_{CaO}/[P\%]_{MgO}\right) = -12760/T + 0.19 \quad (23)$$

where $[P\%]_{CaO}$ is the activity of element P in liquid steel that maken by MgO–CaO crucible; $[P\%]_{MgO}$ is the activity of element P in liquid steel that maken by MgO crucible.

Under the experimental steelmaking temperature (1873 K),

$$\lg[P]_{Ca}/\lg[P]_{Mg} = -3.3113 \quad (24)$$

$$[P]_{Ca}/[P]_{Mg} = 5\times10^{-4} \quad (25)$$

where $[P]_{Ca}$ is the mass fraction of element P in liquid steel that maken by MgO–CaO crucible; $[P]_{Mg}$ is the mass fraction of element P in liquid steel that maken by MgO crucible.

Thus, at the steelmaking temperature, the P content in equilibrium between the molten steel and $Ca_4P_2O_9$ is four orders of magnitude lower than that in equilibrium between the molten steel and $Mg_3(PO_4)_2$. That is, the dephosphorization effect of CaO is much stronger than that of MgO from a thermodynamic viewpoint. Furthermore, CaO can also function as a desulfurization agent and remove Al_2O_3 inclusions, as shown in Eqs. (26)–(31). Obviously, the S, Al, and T.O contents decreased sharply as these reactions proceeded. As a result, the number and size of inclusions decreased substantially, as did the Al_2O_3 content in the inclusions.

$$3CaO(s)_{crucible} + 3[S] + 2[Al] = 3CaS(s)_{inclusions} + Al_2O_3(s)_{incluisons},\ \Delta G^{\ominus} = -879760 + 298.73T\ (J/mol)\ [26] \quad (26)$$

$$CaO(s)_{crucible} + 6Al_2O_3(s)_{incluisons} = CaO\cdot6Al_2O_3(s)_{inclusions},\ \Delta G^{\ominus} = -16380 - 37.58T\ (J/mol)\ [36-37] \quad (27)$$

$$CaO(s)_{crucible} + 2Al_2O_3(s)_{incluisons} = CaO\cdot2Al_2O_3(s)_{inclusions},\ \Delta G^{\ominus} = -15650 - 25.82T\ (J/mol)\ [36-37] \quad (28)$$

$$CaO(s)_{crucible} + Al_2O_3(s)_{incluisons} = CaO\cdot Al_2O_3(l)_{inclusions},\ \Delta G^{\ominus} = -19246 - 18T\ (J/mol)\ [36-37] \quad (29)$$

$$12CaO(s)_{crucible} + 7Al_2O_3(s)_{incluisons} = 12CaO \cdot 7Al_2O_3(l)_{inclusions},\ \Delta G^{\ominus} = 617977 - 612T\ (J/mol)\ [36-37] \quad (30)$$

$$3CaO(s)_{crucible} + Al_2O_3(s)_{incluisons} = 3CaO \cdot Al_2O_3(l)_{inclusions},\ \Delta G^{\ominus} = -11790 - 28.27T\ (J/mol)\ [36-37] \quad (31)$$

The modes of interaction between molten steel and refractories are summarized in Fig. 25.

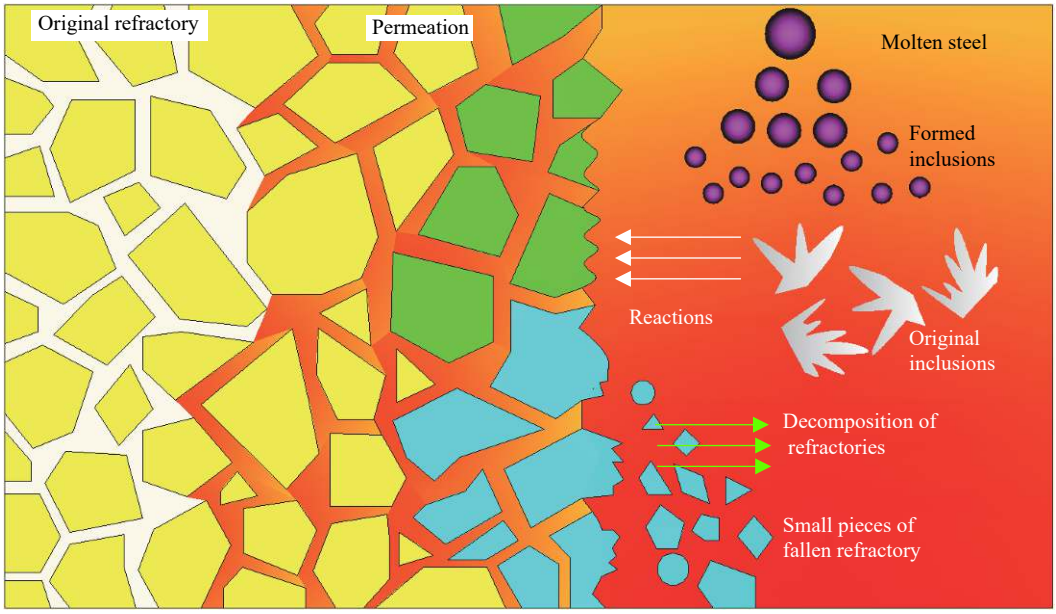

Fig. 25. The modes of interaction between molten steel and refractories: dissolution, permeation, and reaction.

5. Conclusion

Some laboratory experiments were carried out to study the influence of crucible material on inclusions in 95Cr saw-wire steel, the main conclusions are summarized as follows:

(1) The density and average diameter of inclusions in experimental steel decreased gradually with the transition of the oxide from acidic to alkaline in the crucible material (i.e., from SiO_2, Al_2O_3, $MgO \cdot Al_2O_3$, MgO, to MgO–CaO).

(2) In Exp. S, most of the inclusions concentrated in the area with more than 80wt% SiO_2 and the distribution was scattered because the SiO_2 easily reacted with [C], [Mn], and [Ca] in the molten steel.

(3) Inclusions with a high Al_2O_3 content or even composed of pure Al_2O_3 were easily generated when the Al_2O_3-containing crucible was used for steelmaking. This result is mainly attributed to Al_2O_3 in the crucible being easily displaced by [Ca] and [Si] in the molten steel.

(4) The MgO and MgO–CaO crucibles were good choices for smelting low-oxygen, low-$[Al]_s$ 95Cr saw-wire steel, especially the MgO–CaO crucible. The MgO–CaO refractory functioned as a desulfurizer and dephosphorizer, even removing Al_2O_3 inclusions simultaneously. As a result, the content of $[Al]_s$, T.O, P, and S were perfectly controlled within the target range. Furthermore, the number and size of inclusions in the steel samples decreased sharply.

Acknowledgements

The authors are grateful for the support from the National Key Research and Development Program of China (No. 2016YFB0300105), and the Transformation Project of Major Scientific and Technological Achievements in Shenyang (No. Z17-5-003), and the Fundamental Research Funds for the Central Universities (No. N172507002). The authors are grateful to Dr. Lei Xu for his theoretical guidance, who comes from the Institute of Low Carbon and Value Added Metallurgy, School of metallurgy, Northeastern University, China.

References

[1] L.F. Zhang, State of the art in the control of inclusions in tire cord steels — A review, *Steel Res. Int.*, 77(2006), No. 3, p. 158.

[2] M. Hino, Thermodynamics for the control of non-metallic inclusion composition and precipitation, [in] *182th-183th Nishiyama Memorial Seminar*, *ISU*, Tokyo, 2004, p. 1.

[3] P. Zhao and J.D. Boyd, Microstructure-property relationships in thermomechanically processed microalloyed medium carbon steels, *Mater. Sci. Technol.*, 20(2004), No. 6, p. 695.

[4] S. Kobayashi, Thermodynamic fundamentals for alumina-content control of oxide inclusions in Mn–Si deoxidation of molten steel, *ISIJ Int.*, 39(1999), No. 7, p. 664.

[5] Y. Li, C.Y. Chen, Z.H. Jiang, M. Sun, H. Hu, and H.B. Li, Application of alkali oxides in LF refining slag for enhancing inclusion removal in C96V saw wire steel, *ISIJ Int.*, 58(2018),

No. 7, p. 1232.
[6] C.Y. Chen, Z.H. Jiang, Y. Li, M. Sun, G.Q. Qin, C.L. Yao, Q. Wang, and H.B. Li, Effect of Rb_2O on inclusion removal in C96V saw wire steels using low-basicity LF refining slag, *ISIJ Int.*, 58(2018), No. 11, p. 2032.
[7] C.Y. Chen, Z.H. Jiang, Y. Li, M. Sun, K. Chen, Q. Wang, and H.B. Li, Effect of Na_2O and Rb_2O on inclusion removal in C96V saw wire steels using low-basicity LF (Ladle Furnace) refining slags, *Metals*, 8(2018), No. 9, p. 691.
[8] Y.X. Zhu, *Control of Inclusions in Cord Steel* [Dissertation], University of Science and Technology Beijing, 2009, p. 87.
[9] Y.Q. Zhang, *The Study on Morphological Control of Inclusion Using Mg-treatment in Si-Mn Deoxidized Steel* [Dissertation], Northeastern University, 2014, p. 101.
[10] Y. Li, Z.H. Jiang, and Y. Liu, Strengthening mechanism of steels treated by barium-bearing alloys, *J. Univ. Sci. Technol. Beijing*, 15(2008), No. 3, p. 220.
[11] H.Z. Cui and W.Q. Chen, Effect of boron on morphology of inclusions in tire cord steel, *J. Iron Steel Res. Int.*, 19(2012), No. 4, p. 22.
[12] M. Sun, *Effect of Cerium on Inclusions, Microstructure and Mechanical Properties of C104 Saw Wire Steel* [Dissertation], Northeastern University, 2018, p. 78.
[13] K.P. Wang, M. Jiang, X.H. Wang, Y. Wang, H.Q. Zhao, and Z.M. Gao, Formation mechanism of $CaO–SiO_2–Al_2O_3–(MgO)$ inclusions in Si–Mn-killed steel with limited aluminum content during the low basicity slag refining, *Metall. Mater. Trans. B*, 47(2016), No. 1, p. 282.
[14] S.P. Tao and X.C. Zhong, Influence of MgO-based and Al_2O_3-based refractories on inclusions in molten steel, *Iron Steel*, 42(2007), No. 5, p. 33.
[15] C. Ye, *Investigation on Interaction between MgO–A1$_2$O$_3$ Refractory and Molten Steel in Refining Process* [Dissertation], University of Science and Technology Beijing, 2007, p. 103.
[16] H.Q. Zhao and W.Q. Chen, Effect of crucible material and top slag composition on the inclusion composition of tire cord steel, *J. Iron Steel Res.*, 24(2012), No. 3, p. 12.
[17] X.P. He, Q.F. Wang, X.M. Lu, and J.N. Mu, The effect of Al_2O_3 containing refractory on aluminum addition of cord steel, [in] *The 10th National Youth Conference on refractories*, Xi'an, China, 2006, p. 255.
[18] B.X. Wang, D.Y. Guo, and Y.H. Ren, and H. Gao, Effect of submerged entry nozzle material during cord steel continuous casting process on steel property, *Met. Prod.*, 39(2013), No. 5, p. 33.
[19] L. Chen, W. Chen, Y. Hu, Z. Chen, Y. Xu, and W. Yan, Effect of Al antioxidant in MgO–C refractory on the formation of Al_2O_3-rich inclusions in high-carbon steel for saw wire under vacuum conditions, *Ironmaking Steelmaking*, 45(2018), No. 3, p. 272.
[20] M.C. Mantovani, L.R. Moraes, R. Leandro da Silva, E.F. Cabral, E.A. Possente, C.A. Barbosa, and B.P. Ramos, Interaction between molten steel and different kinds of MgO based tundish linings, *Ironmaking Steelmaking*, 40(2013), No. 5, p. 319.
[21] J.X. Chen, *Data Manual of Common Steel Making Charts*, Metallurgical industry press, Beijing, 2010, p. 358.
[22] Z.X. Zhuo, L.F. Wang, X.H. Wang, and W.J. Wang, Composition control of $CaO–SiO_2–Al_2O_3$ inclusion in tire cord steel, *J. Iron Steel Res.*, 17(2005), No. 4, p. 26.
[23] J.F. Elliott and M. Gleiser, *Thermochemistry for Steelmaking*, Addison-Wesley, Massachusetts, 1960, p. 620.
[24] G.K. Sigworth and J.F. Elliott, The thermodynamics of liquid dilute iron alloys, *Met. Sci.*, 8(1974), No. 1, p. 298.
[25] H. Ohta and H. Suito, Activities of MnO in $CaO–SiO_2–Al_2O_3–MnO$ (< 10 pct) $–Fe_tO$ (< 3 pct) slags saturated with liquid iron, *Metall. Mater. Trans. B*, 26(1995), No. 2, p. 295.
[26] G.Z. Ye, P. Jönsson, and T. Lund, Thermodynamics and Kinetics of the Modification of Al_2O_3 Inclusions, *ISIJ Int.*, 36(1996), p. 105.
[27] X.B. Zhang, Thermodynamic modeling for controls of deoxidation and oxide inclusions in molten steel, *Acta Metall. Sin.*, 40(2004), No. 5, p. 509.
[28] H. Cengizler and R.H. Eric, Activity of MnO in $MnO–CaO–MgO–SiO_2–Al_2O_3$ slags at 1500°C, *Steel Res. Int.*, 77(2006), No. 11, p. 793.
[29] R.A. Frank, C.W. Finn, and J.F. Elliott, Physical chemistry of the carbothermic reduction of alumina in the presence of a metallic solvent: Part II. Measurements of kinetics of reaction, *Metall. Mater. Trans. B*, 20(1989), No. 2, p. 161.
[30] M. Ikram-Ul Haq, R. Khanna, Y. Wang, and V. Sahajwalla, A novel X-ray micro-diffraction approach for structural characterization of trace quantities of secondary phases in Al_2O_3–C/Fe system, *Metall. Mater. Trans. B*, 45(2014), No. 6, p. 1970.
[31] R. Khanna, S. Kongkarat, S. Seetharaman, and V. Sahajwalla, Carbothermic reduction of alumina at 1823 K in the presence of molten steel: A sessile drop investigation, *ISIJ Int.*, 52(2012), No. 6, p. 992.
[32] R. Khanna, M. Ikram-Ul Haq, Y. Wang, S. Seetharaman, and V. Sahajwalla, Chemical interactions of alumina–carbon refractories with molten steel at 1823 K (1550°C): Implications for refractory degradation and steel quality, *Metall. Mater. Trans. B*, 42(2011), No. 4, p. 677.
[33] H. Gaye, C. Gatellier, and P.V. Riboud, Physico-chemical aspects of the ladle desulphurization of iron and steel, [in] *Foundry Processes*, Springer, Boston, p. 333.
[34] D.Z. Wang, *Dephosphorization in Iron and Steel Productio*n, Y.J. Cao and J.X. Liu, eds., Metallurgical Industry Press, Beijing, 1986, p. 89.
[35] N. Li and J.C. Kuang, Dephosphorization of basic refractories, *Naihuocailiao*, 34(2000), No. 5, p. 249.
[36] H. Goto, K.I. Miyazawa, and T. Kadoya, Effect of the composition of oxide on the reaction between oxide and sulfur during solidification of steels, *ISIJ Int.*, 35(1995), No. 12, p. 1477.
[37] K. Nagata, J. Tanabe, and K.S. Goto, Activities of calcium oxide in CaO based inclusions measured by galvanic cells, [in] *Proceedings of The Sixth International Iron and Steel Congress*, Nagoya, 1990, p. 217.